technologies

MDPI

Article

In Situ Ceramic Phase Reinforcement via Short-Pulsed Laser Cladding for Enhanced Tribo-Mechanical Behavior of Metal Matrix Composite FeNiCr-B_4C (5 and 7 wt.%) Coatings

Artem Okulov [1,2,*], Olga Iusupova [1], Alexander Stepchenkov [1], Vladimir Zavalishin [1], Elena Marchenkova [1], Kun Liu [3], Jie Li [3], Tushar Sonar [4], Aleksey Makarov [1,2], Yury Korobov [1,2], Evgeny Kharanzhevskiy [5], Ivan Zhidkov [1,2], Yulia Korkh [1], Tatyana Kuznetsova [1,2], Pei Wang [6] and Yuefei Jia [7,8]

1 M.N. Mikheev Institute of Metal Physics, Ural Branch of the Russian Academy of Sciences, Ekaterinburg 620108, Russia; yusupovaolga1@yandex.ru (O.I.); alexander.stepchenkov@gmail.com (A.S.); zavali@imp.uran.ru (V.Z.); elenamarch@imp.uran.ru (E.M.); avm@imp.uran.ru (A.M.); yukorobov@imp.uran.ru (Y.K.); korkh@imp.uran.ru (Y.K.); kuznetsova@imp.uran.ru (T.K.)
2 Institute of Physics and Technology, Ural Federal University, Ekaterinburg 620002, Russia
3 School of Materials Science and Engineering, Jiangsu University of Science and Technology, Zhenjiang 212100, China; liu_kun@163.com (K.L.); lijie081790@hotmail.com (J.L.)
4 Department of Welding Equipment and Technology, Institution of Engineering and Technology, South Ural State University (National Research University), Chelyabinsk 454080, Russia; sonart@susu.ru
5 Department of General Physics, Udmurt State University, Izhevsk 426034, Russia; ehudsuru@gmail.com
6 Henan Key Laboratory of High-Performance Carbon Fiber Reinforced Composites, Institute of Carbon Matrix Composites, Henan Academy of Sciences, Zhengzhou 450046, China; wangpei@hnas.ac.cn
7 Institute of Materials, Shanghai University, Shanghai 200444, China; yuefeijia94@shu.edu.cn
8 Zhejiang Institute of Advanced Materials, Shanghai University, Jiashan 314100, China
* Correspondence: okulovartem@imp.uran.ru

Abstract: This study elucidates the dynamic tribo-mechanical response of laser-cladded FeNiCr-B_4C metal matrix composite (MMC) coatings on AISI 1040 steel substrate, unraveling the intricate interplay between microstructural features and phase transformations. A multi-faceted approach, employing high-resolution scanning electron microscopy (SEM) and advanced X-ray diffraction/Raman spectroscopy techniques, provided a comprehensive characterization of the coatings' behavior under mechanical and scratch testing, shedding light on the mechanisms governing their wear resistance. Specifically, microstructural analysis revealed uniform coatings with a columnar structure and controlled defect density, showcasing an average thickness of 250 ± 20 μm and a transition zone of 80 ± 10 μm. X-ray diffraction and Raman spectroscopy confirmed the presence of α-Fe (*Im-3m*), γ-FeNiCr (*Fm-3m*), Fe_2B (*I-42m*), and B_4C (*R-3m*) phases, highlighting the successful incorporation of B_4C reinforcement. The addition of 5 and 7 wt.% B_4C significantly increased microhardness, showing enhancements up to 201% compared to the B_4C-free FeNiCr coating and up to 351% relative to the AISI 1040 steel substrate, respectively. Boron carbide addition promoted a synergistic strengthening effect between the in situ formed Fe_2B and the retained B_4C phases. Furthermore, scratch test analysis clarified improved wear resistance, excellent adhesion, and a tailored hardness gradient. These findings demonstrated that optimized short-pulsed laser cladding, combined with moderate B_4C reinforcement, is a promising route for creating robust, high-strength FeNiCr-B_4C MMC coatings suitable for demanding engineering applications.

Keywords: Raman spectroscopy; short-pulsed laser cladding; metal matrix composite; boron carbide; microstructural characterization; tribo-mechanical behavior; scratch test

check for updates

Academic Editor: Manoj Gupta

Received: 9 May 2025
Revised: 29 May 2025
Accepted: 3 June 2025
Published: 4 June 2025

Citation: Okulov, A.; Iusupova, O.; Stepchenkov, A.; Zavalishin, V.; Marchenkova, E.; Liu, K.; Li, J.; Sonar, T.; Makarov, A.; Korobov, Y.; et al. In Situ Ceramic Phase Reinforcement via Short-Pulsed Laser Cladding for Enhanced Tribo-Mechanical Behavior of Metal Matrix Composite FeNiCr-B_4C (5 and 7 wt.%) Coatings. *Technologies* **2025**, *13*, 231. https://doi.org/10.3390/technologies13060231

Copyright: © 2025 by the authors. Licensee MDPI, Basel, Switzerland. This article is an open access article distributed under the terms and conditions of the Creative Commons Attribution (CC BY) license (https://creativecommons.org/licenses/by/4.0/).

1. Introduction

The advanced design of metal matrix composite (MMC) coatings is a critical scientific and technological endeavor [1–3]. This is primarily due to the growing demands for increased service life and improved reliability of industrial equipment in modern economic conditions. Austenitic stainless steels (ASSs), based on the FeNiCr system, stand as a distinguished and extensively employed category of materials for durable coatings [4,5]. They are widely used in various industries, including automotive engineering, maritime applications, petroleum processing, water resource management, environmental remediation, and transportation infrastructures [6]. ASSs also play a vital role in demanding applications such as in-core components for nuclear light water reactors, as well as turbine discs and gas compressors [7–10], underscoring the technological significance of these alloys.

ASSs are predominantly composed of iron (Fe), leveraging nickel (Ni), and chromium (Cr) as key alloying additions to tailor structural, phase, and mechanical properties [4–6]. Nickel enhances impact toughness, ductility, and high-temperature strength while simultaneously boosting resistance to corrosive and oxidative degradation. While chromium contributes to increased hardenability, acting as the primary agent for improved corrosion resistance, particularly in oxidizing environments. Such a carefully optimized chemical composition results in a unique set of properties. These properties include exceptional formability, ductility, weldability, non-ferromagnetic behavior, and superior impact toughness at cryogenic temperatures, making ASSs suitable for extreme operational conditions [11]. The face-centered cubic (FCC) crystal structure, which is prevalent in ASSs, dictates fundamental physical, thermal, and mechanical responses [4,12]. Influencing thermal expansion, heat capacity, and plastic deformation behavior, the FCC phase thereby impacts the overall performance in demanding engineering applications.

A promising strategy for enhancing the tribo-mechanical parameters of conventional ASS coatings involves strengthening them by other reinforcing materials. This is achieved through the incorporation of various carbide, boride, and intermetallic phases within their microstructure [13–18]. Specifically, the introduction of ceramic reinforcements into ASSs promotes the in situ formation of novel reinforcing primary and secondary phases. This leads to demonstrable enhancements in both their structural integrity and mechanical performance [14,15]. Among the various ceramic materials, boron carbide (B_4C) is frequently favored. This is due to its superior hardness (47 GPa) compared to a majority of other carbides and borides [19]. The advantageous properties of B_4C include thermodynamic stability and resistance to wear and corrosion [19,20]. Alongside this, its lower relative cost compared to various carbides based on Ti, Zr, Hf, Nb, and W elements [21] contributes to its viability as a cost-effective reinforcement for MCC coatings.

The FeNiCr alloy system, especially in its equiatomic configuration, has garnered significant research interest [16,18,22–26]. As reported in [16,18], equiatomic FeNiCr coatings (3.2 GPa) exhibit a 50% higher microhardness than AISI 1040 steel (2.2 GPa), thereby highlighting their potential for various industrial applications. The addition of 1 and 3 wt.% B_4C to the FeNiCr matrix [16] failed to induce the anticipated in situ formation of iron boride intermetallic compounds (FeB/Fe_2B) and the associated synergistic strengthening effect from the $B_4C/FeB(Fe_2B)$ composite. The Fe_2B phase is preferable to FeB due to the latter's greater brittleness and tendency to form continuous, embrittling networks along grain boundaries, particularly at higher B_4C concentrations. This can significantly reduce ductility and toughness. However, B_4C additions must be carefully controlled, as excessive concentrations can be detrimental to material properties. The increased volume fraction of residual B_4C particles in the matrix, while enhancing hardness, can also act as crack nucleation sites, compromising the overall strength of the composite. Such MMC coatings exhibit increased brittleness, limited load-bearing capacity, and a propensity for premature

failure under stress. In this study, building upon the authors' prior investigations, the B_4C concentration was systematically increased to 5 and 7 wt.% to promote the in situ formation of FeB or Fe_2B intermetallic phases while mitigating any deleterious effects on the coating microstructure and tribo-mechanical behavior.

Achieving optimal microstructure and mechanical performance in MMC coatings requires careful consideration. Effective outcomes depend on both the selection of reinforcement elements, as detailed above, and the chosen deposition technology [27]. Among the established coating techniques, electroplating [28], thermal spraying [29], and laser cladding [30–37] are widely recognized and commercially utilized. Electroplating, known for its cost-effectiveness, suffers from inherent limitations in achievable coating thickness and interfacial bond strength [38]. Thermal spraying, while offering increased operational efficiency, often results in coating-substrate interfaces plagued by defects like porosity and microcracking, potentially leading to premature failure [39]. Laser cladding, conversely, presents benefits such as reduced dilution, a minimized heat-affected zone, and strong metallurgical bonding between the coating and substrate [33], improving overall performance. However, addressing process-inherent defects, particularly solidification cracking [40,41], remains crucial. Ultimately, realizing the full potential of laser cladding for advanced MMC coatings depends on a thorough understanding of the process-structure-property relationships.

This research expands upon the current understanding of laser-cladded MMC FeNiCr-based coatings by examining the synergistic effects of B_4C reinforcement. In this regard, a systematic comparative analysis on the impact of B_4C (5 and 7 wt.%) on microstructure, chemical and phase compositions, and tribo-mechanical behavior was performed. This provided a comprehensive assessment of the advantages and limitations associated with each composition. Informed material selection and optimized coating designs are crucial for specific applications; consequently, this knowledge significantly contributes to extended service life and improved performance in industrial machinery.

2. Materials and Methods

2.1. Powder Materials

Mechanical mixtures of FeNiCr-B_4C powders were prepared using custom-synthesized spherical equiatomic FeNiCr powder (PJSC "Ashinsky Metallurgical Plant", Asha, Russia) as the matrix material and either 5 or 7 wt.% of commercial irregular B_4C powder (LLC IPK "Umex", Ufa, Russia) as the reinforcement phase. The FeNiCr powder exhibited a particle size range of 50–150 μm, while the B_4C powder was characterized by a finer particle size range of 3–5 μm. The chemical compositions (wt.%) of the FeNiCr and B_4C powders are given in Table 1.

Table 1. The chemical compositions of the FeNiCr, B_4C powders, and AISI 1040 steel (wt.%).

Material	Fe	B	Ni	Cr	Mn	C	S	P	Si
FeNiCr	Base	-	35.6	29.8	-	0.37	<0.001	0.008	1.62
AISI 1040 steel		-	-	-	0.6–0.9	0.37–0.44	≤0.05	≤0.04	0.15–0.35
B_4C	-	78.3	-	-	-	21.7	-	-	-

To achieve a homogeneous distribution of the B_4C reinforcement within the FeNiCr matrix, the powder mixtures were subjected to vibratory mixing using a custom-built laboratory setup (UdSU, Izhevsk, Russia). Pre-weighed quantities of the FeNiCr and either 5 or 7 wt.% B_4C powders were combined in a mortar and vibrated continuously for 10 min at a frequency of 50 Hz and an amplitude of 5 mm. These parameters were selected to optimize mixing efficiency while minimizing potential comminution of the powder constituents, thereby yielding a uniformly dispersed composite powder.

2.2. Laser Cladding Process Parameters

Short-pulsed laser cladding was performed using an ytterbium fiber laser system (UdSU, Izhevsk, Russia) to deposit MMC FeNiCr-B_4C coatings (5 and 7 wt.% B_4C) onto an AISI 1040 steel substrate (Table 1, LCC "ANEP-Metal", Ekaterinburg, Russia). Table 2 provides detailed information on the laser cladding parameters.

Table 2. Laser cladding parameters.

Parameter	Value
Material delivery method	Pre-placed powder bed
Shielding gas (Ar), L/min	10
Laser mode	Pulsed
Laser power, W	50
Laser wavelength, μm	1.065
Scanning speed, mm/s	5
Pulse frequency, Hz	20
Pulse duration, ms	3.5
Overlap rate, %	~25
Pulse energy, J	8.3
Pulse energy density, J/cm^2	1057
Laser spot area, cm^2	0.00785
Spot size, mm	1

The optimized laser cladding parameters, carefully selected for this study, promoted a desirable microstructure in the resulting coatings. The pulsed laser mode with a power of 50 W, wavelength of 1.065 μm, pulse frequency of 20 Hz, and pulse duration of 3.5 ms, combined with a scanning speed of 5 mm/s and an overlap rate of ~25%, ensured a controlled energy input. This precise control minimized excessive heat input and promoted localized melting and solidification, leading to a refined grain structure and reduced residual stresses, ultimately enhancing the coating's tribo-mechanical properties and overall performance. The calculated pulse energy of 8.3 J and resulting energy density of 1057 J/cm^2 over a 1 mm spot size provided sufficient energy for adequate powder consolidation and bonding to the substrate without causing significant thermal distortion or unwanted phase transformations. The Ar shielding further minimized oxidation during the process, preserving the desired chemical composition and preventing the formation of undesirable phases. A double-pass cladding strategy was implemented to reduce substrate dilution of the coatings. The resulting coatings exhibited a consistent thickness of 250 $\pm$ 20 μm on specimens with overall dimensions of 5 $\times$ 5 $\times$ 3 mm and a roughness (R_a) of ~1 μm measured using a profilometer model 250 (JSC "Caliber", Moscow, Russia).

2.3. Scanning Electron Microscopy

The microstructure and chemical composition of the FeNiCr-B_4C samples were investigated through a scanning electron microscope (SEM), Tescan MIRA LMS (Tescan Brno S.R.O., Brno, Czech Republic), coupled with energy-dispersive X-ray spectroscopy (EDS) (Oxford Instruments, Abingdon, England) to examine the interfacial characteristics and element distribution.

2.4. X-Ray Diffraction

The XRD analysis of the FeNiCr + 5 wt.% B_4C and FeNiCr + 7 wt.% B_4C coatings was carried out by a Shimadzu XRD-7000 diffractometer (Shimadzu Corporation, Tokyo, Japan) and coupled with a graphite monochromator using CuK_α radiation. The diffraction spectrum was recorded in the angular range $2\Theta = 30–120^\circ$ with the scanning step $\Delta\Theta = 0.03^\circ$

and pulse accumulation for 2 s. The X-ray reflections were identified using the X'Pert HighScorePlus 3.0.5 (Malvern Panalytical, Malvern, UK).

2.5. Raman Spectroscopy

Raman spectroscopy was performed using a Confotec® MR200 confocal microscope (SOL Instruments, Augsburg, Germany) with a 532 nm excitation laser. A laser power of 76 mW was delivered to the sample surface. Spectra were acquired with an integration time of 20 s, averaging 5–10 accumulations per spectral segment to improve the signal-to-noise ratio. Local heating effects were deemed negligible under these conditions. A 40× objective lens (Olympus Corporation, Tokyo, Japan) with a numerical aperture (NA) of 0.75 and a confocal pinhole diameter of 100 µm was employed to achieve high spatial resolution. Scattered light was dispersed using a 1200 lines/mm diffraction grating and detected with an electrically cooled charge-coupled device (CCD).

2.6. Tribo-Mechanical Characterization

Micromechanical measurements and scratch testing (ISO 14577-1:2015 [42]) of laser-cladded FeNiCr-B_4C coatings were performed using a NanoTest-600 system (Micro Materials Ltd., Wrexham, UK) equipped with a Berkovich and a 25 µm radius Rockwell diamond indenters.

(1) Microindentation tests were performed with a loading/holding/unloading time of 20 s each and a maximum load of 250 mN. The vertical and horizontal measurement steps were 50 µm, with a total number of indenter prints of 200 for each coating. The measurement error was determined using standard deviation with a confidence probability of 0.95.

(2) The scratch testing procedure involved creating three scratches per specimen under a constant load of 250 mN and a velocity of 2 µm/s, with scratch lengths of 300–340 µm. A pre-test scratch (1 mN load, 10 µm length) was performed before each test. Surface topography scans (1 mN load) were conducted before and after scratching to evaluate the initial surface condition and measure residual scratch depth. Prior to scratch testing, cross-sections of the specimens were polished to minimize surface roughness effects. The resulting scratches were then analyzed via SEM to identify the dominant failure mechanisms.

3. Results and Discussion

3.1. Microstructure and Chemical Composition

Figure 1 shows the schematic illustration of a short-pulsed laser cladding process and the phase formation of the FeNiCr + B_4C powder mixture after laser exposure (according to X-ray diffraction/Raman spectroscopy-based analyses provided below).

As shown in Figure 1b, the laser cladding process involves a complex interplay of physical phenomena within the process zone, including thermal conduction, thermocapillary flow (Marangoni effect), powder and shield gas forces on melt pool, mass transport, diffusion, laser/powder, melt pool/powder, and laser/substrate interactions [33]. According to the X-ray diffraction/Raman spectroscopy-based analyses, this led to the formation of the corresponding α-Fe, γ-FeNiCr, Fe_2B and B_4C phases. The SEM analysis of the custom spherical FeNiCr powder confirmed the fraction of 50–150 µm and the chemical composition close to the equiatomic one, according to the manufacturer's test certificate (Figure 1c). The purity (99.6%) and fraction (3–5 µm) of the commercial irregular-shaped B_4C powder used in this study also met the manufacturer's specifications (Figure 1d). A general view of the manufactured FeNiCr + 5 wt.% B_4C and FeNiCr + 7 wt.% B_4C samples is shown in Figure 1e.

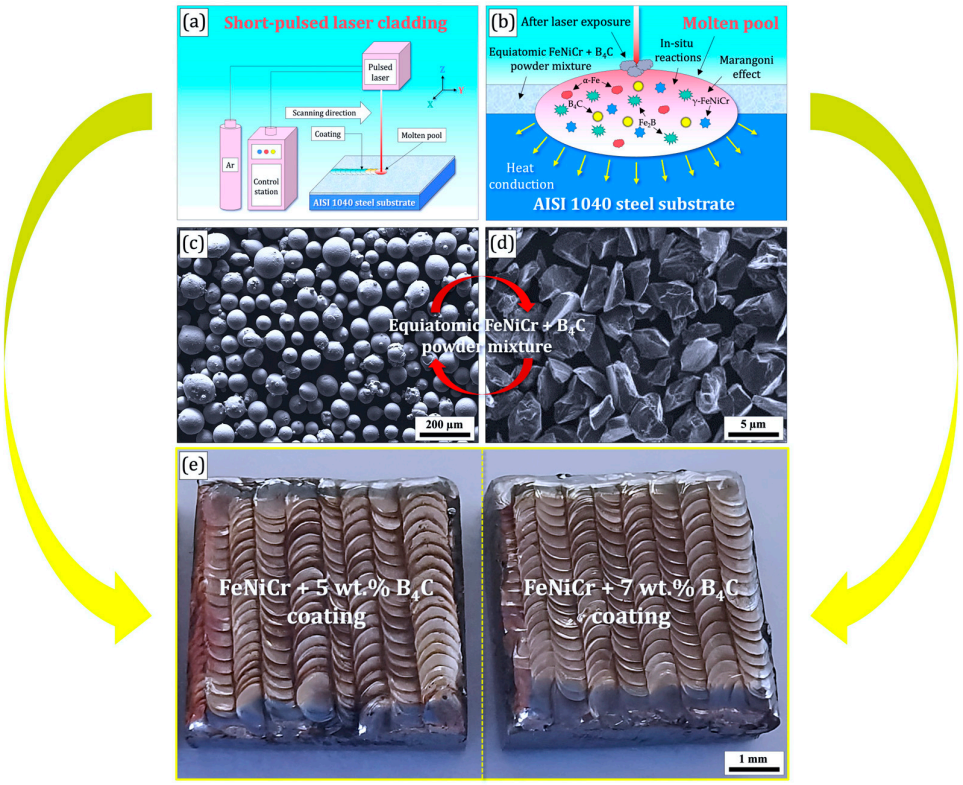


Figure 1. Schematic illustration of the (**a**) short-pulsed laser cladding process and (**b**) phase formation of the FeNiCr + B_4C powder mixture after laser exposure (according to X-ray diffraction/Raman spectroscopy-based analyses). General view of the (**c**) FeNiCr and (**d**) B_4C feedstock powders, (**e**) manufactured FeNiCr + 5 wt.% B_4C and FeNiCr + 7 wt.% B_4C samples.

The SEM-based microstructural characterization of both synthesized FeNiCr-B_4C (5 and 7 wt.% B_4C) coatings revealed that their cross-sections, etched with HNO_3, possess a homogeneous surface texture with a typical column structure (Figure 2e,j) and rare defects such as elongated (Figure 2h) and keyhole pores (Figure 2c,h), as well as cracks (Figure 2h). A significant decrease in the size of indentation marks is observed in Figure 2b,g. This indicates a noticeable increase in the microhardness values of these areas.

The elemental mapping of the FeNiCr + 5 wt.% B_4C and FeNiCr + 7 wt.% B_4C cross-sections (Figure 2a,f) clearly demonstrates the transition (remelting) zones between the substrate and coating materials. The transition zones are especially visible on the Fe mappings, as indicated by horizontal arrows on the inserts. The average thickness of both coatings is 250 ± 20 µm. Table 3 shows the chemical composition of the selected coating areas (Figure 2d,i).

Table 3. The chemical composition of laser-cladded FeNiCr-B_4C (5 and 7 wt.% B_4C) coatings (wt.%).

Sample	Fe	Ni	Cr	B	C
FeNiCr + 5 wt.% B_4C	33.45	31.26	29.04	4.65	1.60
FeNiCr + 7 wt.% B_4C	31.56	29.52	30.23	6.75	1.94

The data obtained confirm that the coatings retain a near-equiatomic composition, closely mirroring that of the original custom-synthesized FeNiCr powder. Furthermore, the implementation of a short-pulsed laser cladding process facilitates the creation of coatings with uniform thickness and a homogeneous microstructure. This suggests that the laser cladding parameters were optimized to minimize elemental segregation and

promote consistent solidification, leading to a high-quality coating with predictable and reliable properties.

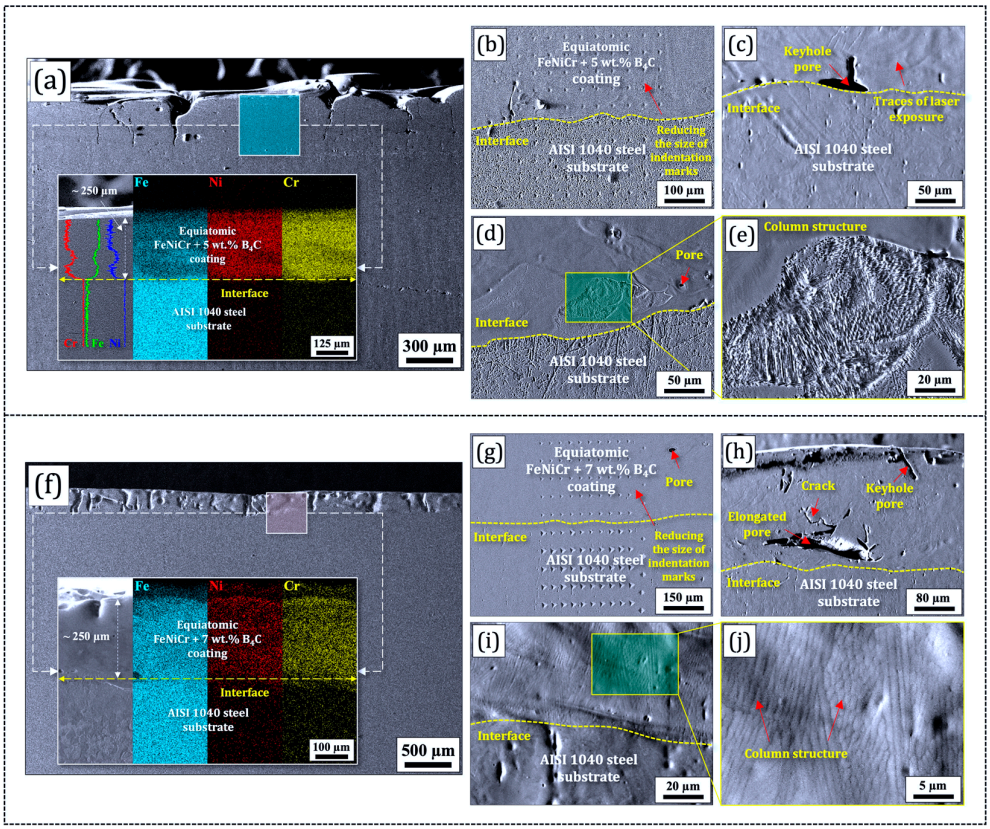


Figure 2. General view of the (**a**) FeNiCr + 5 wt.% B_4C and (**f**) FeNiCr + 7 wt.% B_4C cross-sections with their most informative (**b**–**e**) and (**g**–**j**) microstructural areas, respectively.

3.2. X-Ray Diffraction Analysis

According to the X-ray diffraction (XRD) analysis presented in Figure 3, the phase composition of both FeNiCr-B_4C (5 and 7 wt.% B_4C) coatings was determined to consist of α-Fe (space group *Im-3m*) [43], γ-FeNiCr (space group *Fm-3m*) [22–26], Fe_2B (space group *I-42m*) [44,45], and B_4C (space group *R-3m*) phases [19,46].

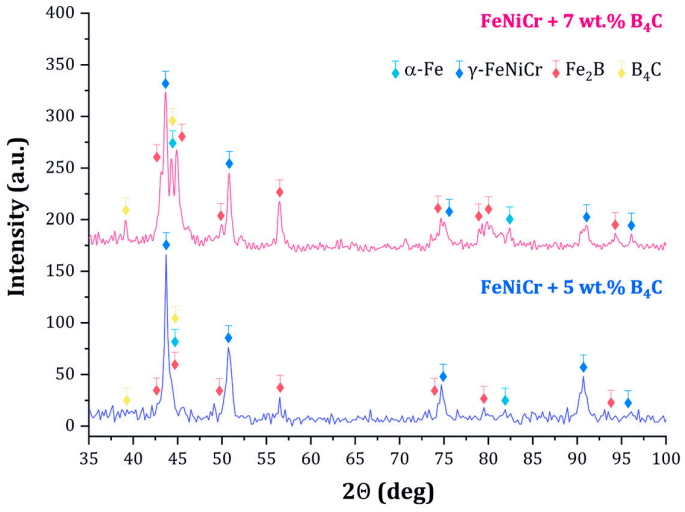


Figure 3. XRD patterns of the FeNiCr + 5 wt.% B_4C and FeNiCr + 7 wt.% B_4C coatings.

The observed intensity distributions of the XRD spectra were noticeably influenced by the preferred crystallographic orientation, or texture, of the crystallites within each sample. This texturing effect is evident, as the integral intensities of the Bragg peaks, particularly those associated with the Fe_2B and B_4C phases, were more pronounced in the FeNiCr + 7 wt.% B_4C coating compared to the FeNiCr + 5 wt.% B_4C coating. Such variations in peak intensities suggest differences in the volume fractions and/or crystallographic orientations of these phases between the coatings. Furthermore, the diffraction lines corresponding to all observed phases exhibited significant broadening. This broadening is indicative of a highly defective crystal structure, incorporating, for example, internal stresses, and the presence of numerous dislocations and/or small crystallite sizes, which are all known to contribute to peak broadening in XRD patterns. The observed broadening provides direct evidence of the non-equilibrium solidification kinetics inherent in the laser cladding process, and, consequently, a refinement of the grain size and a high density of lattice defects. These structural features played a dominant role in shaping the tribo-mechanical performance of the coatings.

The phase composition of laser-cladded FeNiCr-B_4C (5 and 7 wt.% B_4C) coatings with calculated unit cell parameters is presented in Table 4.

Table 4. The phase composition and unit cell parameters of laser-cladded FeNiCr-B_4C (5 and 7 wt.% B_4C) coatings.

Sample	Phase	Unit Cell Parameters, Å		
		a	**c**	**V**
FeNiCr-B_4C (5 and 7 wt.% B_4C)	α-Fe, *Im-3m*	2.87	-	23.64
	γ-FeNiCr, *Fm-3m*	3.591	-	46.31
	Fe_2B, *I-42m*	5.078	4.223	108.89
	B_4C, *R-3m*	5.60	12.12 (120°)	329.16

Rietveld refinement quantified the phase compositions of both coatings. The FeNiCr + 5 wt.% B_4C coating consisted of 3.1% α-Fe, 80.3% γ-FeNiCr, 7% B_4C, and 9.6% Fe_2B, while the FeNiCr + 7 wt.% B_4C coating comprised 4.6% α-Fe, 72% γ-FeNiCr, 10.4% B_4C, and 13% Fe_2B. These phase ratios, notably the increased presence of B_4C and Fe_2B, were achieved through the controlled addition of B_4C and optimization of the laser thermal profile. Increasing the B_4C concentration to 5 and 7 wt.% directly impacts the available boron, driving the formation of Fe_2B intermetallic phases, as evidenced by the observed XRD patterns. Concurrently, the laser thermal profile, determined by parameters such as power, scanning speed, and pulse duration, governs the local temperature distribution and cooling rates during the laser cladding process. These thermal conditions dictate the kinetics of phase transformations, affecting the size, morphology, and distribution of both B_4C and Fe_2B phases within the FeNiCr matrix. For example, a higher energy input promotes more extensive melting and mixing, potentially leading to more uniform phase distributions, while faster cooling rates may favor the formation of finer microstructures. By carefully controlling both the B_4C content and the laser parameters, we successfully tailored the phase composition and microstructure, thereby achieving optimized tribo-mechanical properties of the FeNiCr-B_4C coatings.

Summarizing the above findings, the addition of 5 and 7 wt.% B_4C to the FeNiCr matrix resulted in reinforcement by in situ formed Fe_2B and retained B_4C phases, which directly contributed to the observed superior microhardness. In addition to the bulk phase identification by XRD, Raman spectroscopy was employed to investigate the distribution and bonding characteristics of B_4C and the newly formed Fe_2B within the FeNiCr-B_4C coatings.

3.3. Raman Spectroscopy Analysis

The characteristic surface areas named spots 1 (grey areas), 2 (white areas), 3 (dark areas), and microdrops were chosen on the surface of the FeNiCr-B_4C (5 and 7 wt.% B_4C) coatings for Raman spectra detection. Optical images of the above detection spots are shown using FeNiCr + 5 wt.% B_4C coating as an example (Figure 4). The Raman spectra measured on the present FeNiCr + 5 wt.% B_4C and FeNiCr + 7 wt.% B_4C coatings, as well as the AISI 1040 steel substrate and the previously reported FeNiCr-B_4C (0, 1 and 3 wt.% B_4C) coatings [16], are shown in Figure 4a–d. Figure 4 demonstrates the difference in the intensity of the Raman bands between different detection spots. The Raman peaks, averaged over 5–7 spectra, were identified at each detection spot for all the samples. The interpretation of the Raman spectra is presented in Table 5.

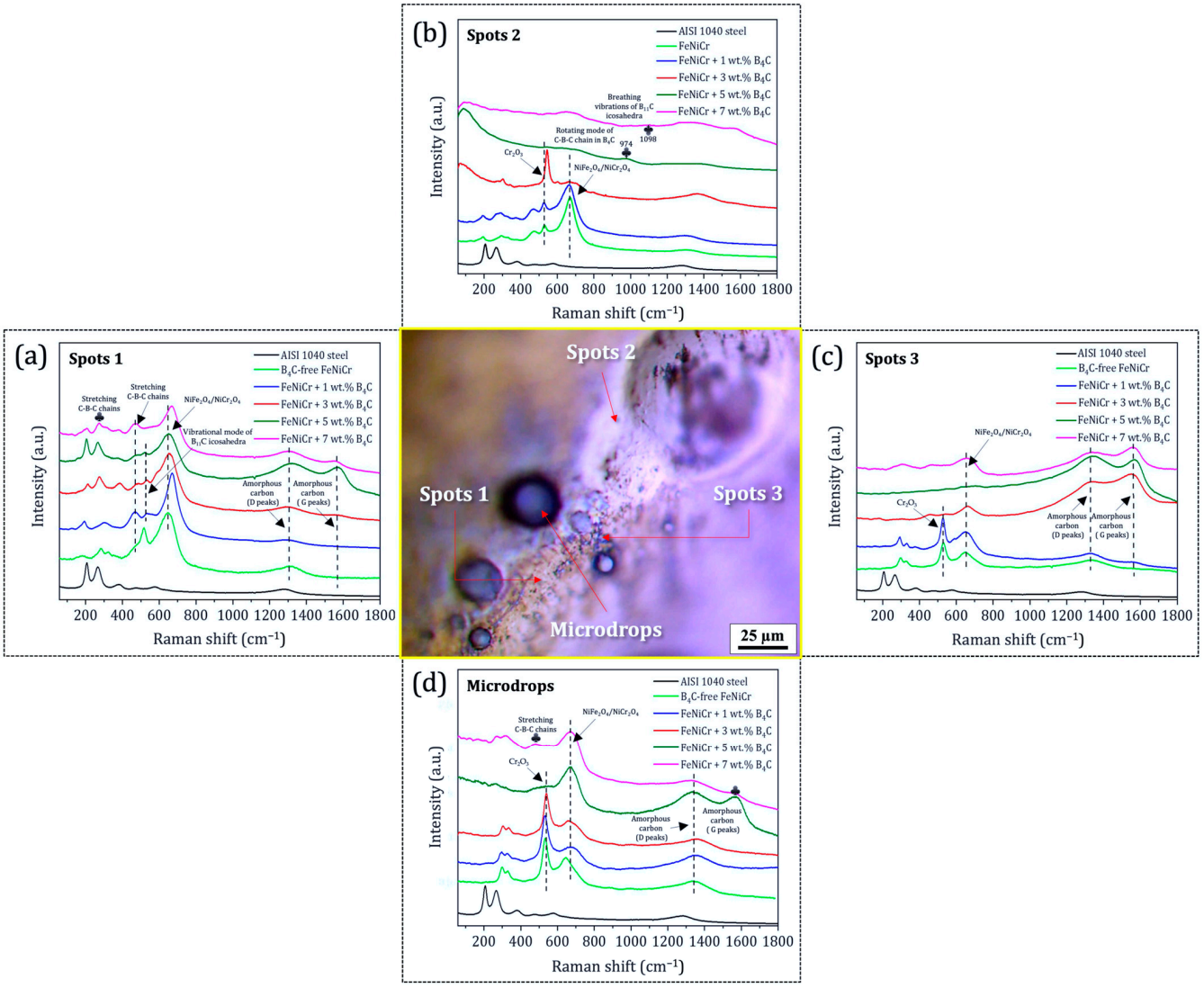


Figure 4. Optical image of the spots 1 (grey areas), spots 2 (white areas), spots 3 (dark areas), and microdrops of Raman spectra for the FeNiCr + 5 wt.% B_4C coating as an example. Comparative Raman spectra of the AISI 1040 steel substrate and FeNiCr-B_4C (0, 1, 3 [16], 5, and 7 [this study] wt.% B_4C) coatings are marked as: (**a**) spots 1, (**b**) spots 2, (**c**) spots 3, and (**d**) microdrops. The dashed lines visually identify the shift of Raman peaks for the FeNiCr-B_4C coatings.

Table 5. The average peak positions of the Raman spectra detected for different surface spots: AISI 1040 steel substrate and FeNiCr-B_4C (0, 1, 3 [16], 5, and 7 [this study] wt.% B_4C) coatings.

AISI 1040 Steel	FeNiCr-B_4C Coatings					Interpretation
	0 wt.% B_4C	1 wt.% B_4C	3 wt.% B_4C	5 wt.% B_4C	7 wt.% B_4C	
207	196	194	209	205	208	α-Fe_2O_3
267	293	279	273	267	271	α-Fe_2O_3
-	-	-	-	-	320	Stretching C-B-C chains in B_4C
380	-	377	383	376	378	γ-Fe_2O_3
-	-	469	478	472	462	Stretching C-B-C chains in B_4C
480	477	-	-	-	-	NiO
-	518	-	-	-	-	Fe_3O_4
-	-	533	532	523	-	Vibrational mode of $B_{11}C$ icosahedra
-	527	528	543	530	-	Cr_2O_3
-	-	-	-	-	556	Vibrational mode of $B_{11}C$ icosahedra
578	-	-	-	-	-	γ-Fe_2O_3
645	648	-	-	-	-	γ-Fe_2O_3
-	672	665	657	654	667	$NiFe_2O_4$/$NiCr_2O_4$
-	-	-	-	-	897	Intraicosahedral B-B bonds
-	-	-	-	974	-	Rotating mode of C-B-C chain in B_4C
-	-	-	-	-	1098	Breathing vibrations of $B_{11}C$ icosahedra
1280	-	-	-	-	-	α-Fe_2O_3
-	1330	1328	1330	1330	1332	Amorphous carbon (D peak)
-	-	1560	1554	1572	1562	Amorphous carbon (G peak)

As previously reported in [16], the Raman spectra detected on the FeNiCr-B_4C (0, 1, and 3 wt.% B_4C) coatings sufficiently differed from the spectra of the AISI steel substrate, which also corresponded to the present FeNiCr + 5 wt.% B_4C and FeNiCr + 7 wt.% B_4C coatings presented in this study. The most prominent Raman peaks of the AISI steel substrate corresponded to α-Fe_2O_3 phase [47], whereas the FeNiCr-B_4C (0, 1, 3, 5, and 7 wt.% B_4C) coatings were characterized by the lower-intensity iron oxide (α-Fe_2O_3, γ-Fe_2O_3) peaks, and the intense peaks at 527–543 cm^{-1} and 654–672 cm^{-1} corresponding to the Cr_2O_3 and $NiCr_2O_4$ phases [48], respectively.

The appearance of Raman peaks at 320, 462–478 cm^{-1} corresponding to the stretching of C-B-C chains in B_4C and the 974 cm^{-1} peak attributed to the rotating mode of C-B-C chain in B_4C [49–51] were found only for the FeNiCr-B_4C (1, 3, 5, and 7 wt.% B_4C) coatings. It should be noted that the intensity of peaks corresponding to the characteristic oscillations of the C-B-C chains in B_4C was higher for the coating reinforced with 7 wt.% B_4C, which confirmed a higher concentration of B_4C carbides inside the FeNiCr + 7 wt.% B_4C coating among the other ones. The 462–478 cm^{-1} peak maxima were shifted to lower frequencies for coatings with 5 and 7 wt.% B_4C, which indicated a higher in-plane strain in the FeNiCr-B_4C coating with higher B_4C content. Additional Raman peaks at 523–533, 556 cm^{-1}, attributed to the vibrational mode of $B_{11}C$ icosahedra [49], appeared in the FeNiCr-B_4C (1, 3, 5 and 7 wt.% B_4C) coatings. The Raman peaks at 897 and 1098 cm^{-1}, related to intraicosahedral B–B bonds and breathing vibrations of $B_{11}C$ icosahedra [49], respectively, were found only for

the FeNiCr + 7 wt.% B_4C coating, which was associated with a higher concentration of B_4C in this sample. The high-intensity peaks at 1328–1332 cm^{-1} corresponding to amorphous carbon (D peaks) were detected for all the FeNiCr-B_4C (0, 1, 3, 5, and 7 wt.% B_4C) coatings, while the 1554–1572 cm^{-1} peaks (G peaks) attributed to the presence of free carbon in B_4C were found only for the FeNiCr-B_4C (1, 3, 5, and 7 wt.% B_4C) ones, which additionally confirmed the presence of B_4C carbides in these samples.

By means of different surface spots taken for measuring Raman spectra (Figure 4), it was found that peaks corresponding to α-Fe_2O_3 (206, 270 cm^{-1}) were detected only for spot 1. The broader peak at 668 cm^{-1} for spot 1, corresponding to $NiCr_2O_4$ phase, indicated a more stressed state in the FeNiCr + 7 wt.% B_4C coating compared to the FeNiCr-B_4C (1, 3 and 5 wt.% B_4C) ones. Spot 2 could be characterized by a lower content of the $NiCr_2O_4$ phase inside the FeNiCr-B_4C (3, 5, and 7 wt.% B_4C) coatings, while spot 1 and microdrops were associated with more intense peaks of the $NiCr_2O_4$ phase for all the FeNiCr-B_4C samples. The dark areas (spots 3) of all the FeNiCr-B_4C coatings were characterized by high-intensity peaks corresponding to amorphous carbon, which indicated a higher content of B_4C carbides in them. The Raman peaks related to the rotating mode of the C-B-C chain in B_4C and breathing vibrations of $B_{11}C$ icosahedra were detected only for spots 2 (white areas).

3.4. Mechanical Characterization

As detailed in Figure 5 and Table 6, the average instrumented microhardness (H_{IT}) values for the laser-cladded FeNiCr + 5 wt.% B_4C and FeNiCr + 7 wt.% B_4C coatings were approximately 8.1 GPa and 9.7 GPa, respectively. This represents a substantial 20% increase in microhardness with the higher B_4C content. Furthermore, the obtained results clearly demonstrate a significant enhancement in microhardness resulting from the 5 and 7 wt.% B_4C reinforcement, compared to previously reported values for equiatomic FeNiCr coatings without B_4C [16,18] and the AISI 1040 steel substrate. Specifically, the microhardness of the FeNiCr + 5 wt.% B_4C and FeNiCr + 7 wt.% B_4C coatings exhibited a 151% and 201% improvement, respectively, relative to the B_4C-free FeNiCr coating, and a 276% and 351% improvement, respectively, compared to the AISI 1040 steel substrate. This significant increase in hardness can be attributed to a synergistic combination of strengthening mechanisms. These include solid solution strengthening from the alloying elements, grain refinement induced by the rapid solidification inherent in laser cladding, and, most notably, in situ precipitation strengthening from the formation of hard Fe_2B phases and the presence of retained B_4C phases. Increased B_4C content in the 7 wt.% B_4C coating further facilitates the formation and distribution of these strengthening phases, thereby accounting for the observed higher microhardness compared to the 5 wt.% B_4C coating.

The microhardness profiles (Figure 5a) effectively differentiate the coating layers, which exhibit negligible mixing with the AISI 1040 steel substrate, from the compositional transition zones where significant intermixing is evident. The average coating thickness, validated by these profiles, is ~250 μm, with the compositional transition zones measuring ~80 μm. Moreover, subtle deviations in microhardness values are observed within both the coating and transition zones. These localized variations likely stem from the heterogeneous redistribution of B_4C and Fe_2B phases during the rapid solidification associated with the laser cladding process. This uneven distribution results in regions enriched in these hard phases, leading to localized increases in microhardness, while regions depleted of these phases exhibit correspondingly lower values. Therefore, the microhardness profiles provide valuable insights into the microstructural homogeneity and phase distribution within the composite coatings.

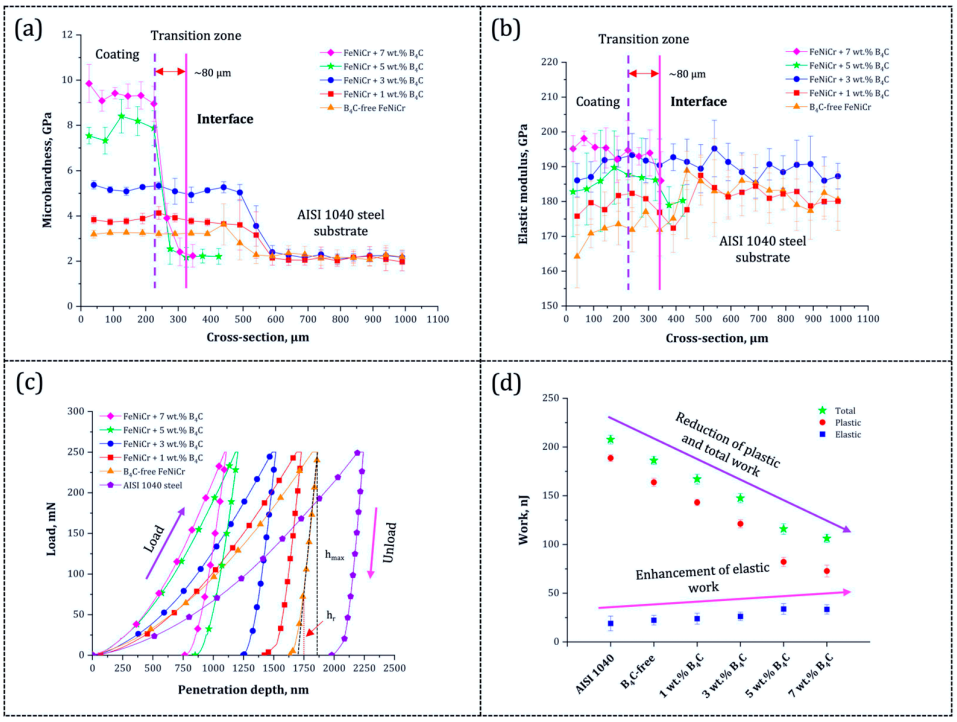


Figure 5. Mechanical characterization of the AISI 1040 steel substrate and FeNiCr-B_4C (0, 1, 3 [16], 5 and 7 [this study] wt.% B_4C) coatings: (**a**) microhardness, (**b**) elastic modulus, (**c**) loading/unloading curves, and (**d**) work (elastic, plastic, and total) graphs.

Table 6. Mechanical characteristics of the AISI 1040 steel substrate and FeNiCr-B_4C (0, 1, 3 [16], 5 and 7 [this study] wt.% B_4C) coatings.

Material	Work, nJ			H_{IT}, GPa	E^*, GPa	H_{IT}/E^*	H_{IT}^3/E^{*2}, GPa	R_e, %	δ_A
	Total	Plastic	Elastic						
AISI 1040 steel	206.81	188.79	18.02	2.154	184.68	0.0117	0.0003	3.85	0.90
B_4C-free FeNiCr	186.14	163.84	22.30	3.228	172.11	0.0188	0.0011	5.90	0.86
FeNiCr + 1 wt.% B_4C	167.04	143.15	23.89	3.825	178.34	0.0214	0.0018	6.60	0.83
FeNiCr + 3 wt.% B_4C	147.50	121.22	26.28	5.167	190.64	0.0271	0.0038	8.30	0.78
FeNiCr + 5 wt.% B_4C	115.95	82.16	33.79	8.091	181.01	0.0447	0.0162	13.70	0.59
FeNiCr + 7 wt.% B_4C	106.23	72.79	33.44	9.711	201.17	0.0483	0.0226	14.54	0.54
Comparative analysis (change (↓↑) in %)									
7 wt.% B_4C vs. 5 wt.% B_4C	8 ↓	11 ↓	1 ↓	20 ↑	11 ↑	8 ↑	40 ↑	6 ↑	8 ↓
5 wt.% B_4C vs. B_4C-free	38 ↓	50 ↓	52 ↑	151 ↑	5 ↑	138 ↑	1373 ↑	132 ↑	31 ↓
7 wt.% B_4C vs. B_4C-free	43 ↓	56 ↓	50 ↑	201 ↑	17 ↑	157 ↑	1955 ↑	146 ↑	37 ↓
5 wt.% B_4C vs. AISI 1040 steel	44 ↓	56 ↓	88 ↑	276 ↑	2↓	282 ↑	5300 ↑	256 ↑	34 ↓
7 wt.% B_4C vs. AISI 1040 steel	49 ↓	61 ↓	86 ↑	351 ↑	9 ↑	313 ↑	7433 ↑	278 ↑	40 ↓

The effective elastic modulus (E^*), as depicted in Figure 5b, reveals that the FeNiCr + 7 wt.% B_4C coating exhibits a superior stiffness, with E^* values exceeding those of the FeNiCr + 5 wt.% B_4C coating, AISI 1040 steel substrate, and B_4C-free FeNiCr coating by 11%, 9%, and 17%, respectively. Conversely, the E^* value of the FeNiCr + 5 wt.% B_4C coating is closely aligned (within ~2%) with that of the AISI 1040 steel substrate and demonstrates a 5% increase compared to the B_4C-free FeNiCr coating. The elevated E^* value observed for the FeNiCr + 7 wt.% B_4C coating signifies its enhanced resistance to elastic deformation [52,53], suggesting improved dimensional stability and load-bearing capacity relative to the other materials under consideration.

The loading/unloading curves, illustrated in Figure 5c, effectively demonstrate the impact of B_4C particle reinforcement on the mechanical response of the equiatomic FeNiCr coating. These curves, representing the average behavior across multiple indentations, reveal a marked reduction in the maximum indentation depth (h_{max}) for both the FeNiCr + 5 wt.% B_4C (1206.81 nm) and FeNiCr + 7 wt.% B_4C (1114.67 nm) coatings compared to the B_4C-free FeNiCr coating (1877.43 nm) and the AISI 1040 steel substrate (2146.02 nm). Furthermore, the residual depth (h_r), which represents the point of intersection between the tangent and the unloading curve, provides insight into the elastic recovery behavior of the materials. A lower h_r value signifies a greater degree of elastic recovery [54–56], and the FeNiCr + 7 wt.% B_4C coating exhibits the lowest h_r value (952.3 nm), indicating the most pronounced elastic recovery among the materials tested (Figure 5c). This suggests that the FeNiCr + 7 wt.% B_4C coating possesses a superior ability to resist permanent deformation under load.

The elastic, plastic, and total work values were determined from the areas under the loading and unloading segments of the nanoindentation curves (Figure 5d). An analysis reveals that the FeNiCr + 5 wt.% B_4C and FeNiCr + 7 wt.% B_4C coatings exhibit contrasting behavior compared to both the AISI 1040 steel substrate and the B_4C-free FeNiCr coating: a decrease in both plastic and total work, accompanied by an increase in elastic work (Figure 5d, Table 6). Furthermore, the 7 wt.% B_4C coating demonstrates superior mechanical properties compared to the 5 wt.% B_4C coating. This is evidenced by the 8% higher H_{IT}/E^* ratio, a 40% higher $H_{IT}{}^3/E^{*2}$ ratio, and a 6% higher R_e value, collectively signifying a greater resistance to plastic deformation and improved wear resistance. Compared to the B_4C-free FeNiCr coating, the FeNiCr + 5 wt.% B_4C coating displays a significant increase in the H_{IT}/E, $H_{IT}{}^3/E^{*2}$, and R_e parameters, rising by 138%, 1373%, and 132%, respectively. The FeNiCr + 7 wt.% B_4C coating also exhibits improvements, with increases of 157%, 1955%, and 146% in the same parameters. These substantial increases in H_{IT}/E and $H_{IT}{}^3/E^{*2}$ underscore the enhanced stiffness and improved resistance to plastic deformation and wear, as per the established literature [52,53]. The observed elevation in the R_e parameter also confirms the enhanced capacity of the B_4C-reinforced coatings to elastically withstand mechanical stress up to the point of plastic deformation [55–57].

Conversely, the plasticity index (δ_A) exhibits a reduction in the B_4C-reinforced coatings. Specifically, the δ_A values for the FeNiCr + 5 wt.% B_4C and FeNiCr + 7 wt.% B_4C coatings are reduced by 31% and 37%, respectively, compared to the B_4C-free FeNiCr coating, and by 34% and 40%, respectively, compared to the AISI 1040 steel substrate material. This reduction in δ_A confirms the increased hardening of the coatings resulting from the incorporation of B_4C particles, with a more pronounced effect observed in the FeNiCr + 7 wt.% B_4C coating. The lower plasticity index signifies a reduced tendency for plastic deformation and an increased propensity for elastic behavior under applied stress.

3.5. Scratch Test Assessment

Scratch test analysis of the FeNiCr-B_4C (5 and 7 wt.% B_4C) cross-sections is shown in Figure 6. This provided a comprehensive assessment by collecting quantitative data (average scratch depth and width) and conducting qualitative analysis (visual assessment of deformation morphology) for both the coatings and the AISI 1040 steel substrate. Topographical profiles on the FeNiCr-B_4C cross-sections (Figure 6a,g) revealed a gradual increase in penetration depth as the indenter moved from the coating to the substrate. The observation suggests both good adhesion and hardness gradient, attributed to B_4C reinforcement of the FeNiCr matrix. This behavior shows that the coatings effectively support the load, resisting penetration better than the AISI 1040 steel substrate.

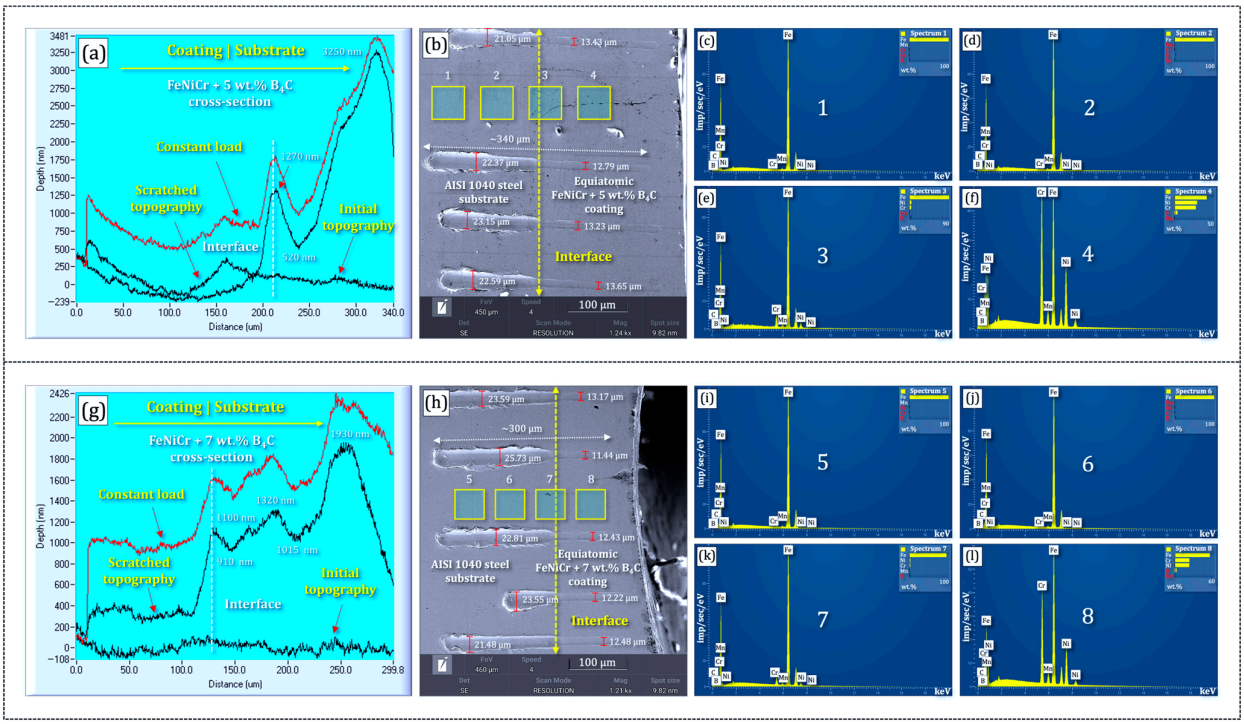


Figure 6. Scratch test analysis of the FeNiCr-B_4C (5 and 7 wt.% B_4C) cross-sections: (**a**,**g**) penetration depth/distance graphs, and (**b**,**h**) scratch morphology for both samples, respectively; EDS analysis for selected FeNiCr + 5 wt.% B_4C (**c**) 1, (**d**) 2, (**e**) 3, (**f**) 4, and FeNiCr + 7 wt.% B_4C (**i**) 5, (**j**) 6, (**k**) 7, (**l**) 8 areas.

The penetration depth/distance graphs (Figure 6a,g) show a distinct transition at the coating/substrate interface, marked by an abrupt change in depth as the indenter passes from the coating to the substrate. While the relatively uniform penetration depth profile across the coating suggests a constant resistance to deformation, implying a controlled level of ductility, the substrate exhibits significant fluctuations in the scratch curve. The SEM analysis (Figure 6b,h) confirmed this differential behavior. A quantitative assessment of the scratch profiles clarified an average scratch thickness within the substrate region of 22.29 nm for the FeNiCr + 5 wt.% B_4C sample and 23.43 nm for the FeNiCr + 7 wt.% B_4C sample. In contrast, the average scratch thickness within the coating layer was markedly reduced, measuring 13.28 nm and 12.35 nm for the FeNiCr + 5 wt.% B_4C and FeNiCr + 7 wt.% B_4C samples, respectively. Both the FeNiCr-B_4C coatings show uniform, narrow scratches without delamination or defects, indicating a predominantly elastic deformation regime with limited plastic flow under the applied load. This suggests that the coatings possess a higher yield strength and are more prone to elastic recovery, resulting in a shallower, more uniform groove. In contrast, the substrate shows non-uniform scratch widening accompanied by delamination at the edges. The latter observations indicate greater ductility; a lower yield strength results in greater plastic deformation and possibly lower fracture toughness, resulting in the observed delamination. The inconsistent penetration depth and pronounced scratch widening in the substrate indicate a non-uniform material response and a greater propensity to plastic deformation under the applied stress compared to the more elastically resistant and homogeneous coating.

EDS mapping of the cross-sections (Figure 6c–f,i,j) further elucidated the spatial variation in elemental composition within the FeNiCr-B_4C (5 and 7 wt.% B_4C) samples. This compositional information, combined with the visual assessment of scratch depth (Figure 6a,g) and thickness (Figure 6b,h) variations, provides a reliable method for precisely defining the coating-substrate interface. The correlation of EDS data with mechanical

scratch behavior allows for a comprehensive understanding of the coating's structure and adherence to the substrate.

In summary, the comprehensive scratch test analysis, incorporating topographical profiling, quantitative measurements, and morphological assessment, confirmed the enhanced wear resistance and superior mechanical properties of the FeNiCr-B_4C coatings. These coatings exhibit excellent adhesion, a beneficial hardness gradient, high cohesive strength, a degree of plasticity, and homogenous B_4C dispersion, all contributing to their overall durability and making them suitable for demanding applications.

4. Conclusions

This research aimed to evaluate the potential of laser-cladded FeNiCr-based MMC coatings reinforced with moderate concentrations of B_4C (5 and 7 wt.%). The coatings were systematically studied by a comparative analysis of their microstructure, phase composition, and tribo-mechanical properties. The following key results were obtained:

(1) The FeNiCr-B_4C (5 and 7 wt.% B_4C) cross-sections are characterized by an average thickness of 250 $\pm$ 20 μm and a transition zone of 80 $\pm$ 10 μm. Both coatings possess a homogeneous surface texture with a typical column structure and rare defects, such as elongated and keyhole pores, as well as cracks.

(2) The XRD analysis confirmed that both FeNiCr-B_4C (5 and 7 wt.% B_4C) coatings consist of the following phases: α-Fe, space group *Im-3m*; γ-FeNiCr, space group *Fm-3m*; Fe_2B, space group *I-42m*; and B_4C, space group *R-3m*.

(3) Raman spectroscopy also revealed the presence of B_4C phases inside the FeNiCr + 5 wt.% B_4C and FeNiCr + 7 wt.% B_4C coatings through detected peaks corresponding to amorphous carbon, stretching C-B-C chains in B_4C and vibrational modes of $B_{11}C$ icosahedra. The additional peaks related to intraicosahedral B-B bonds, rotating mode of the C-B-C chain in B_4C, and breathing vibrations of $B_{11}C$ icosahedra were identified for both presented coatings. This was an extra indicator of the B_4C presence.

(4) In situ reinforcement with 5 and 7 wt.% B_4C significantly increased microhardness, showing enhancements up to 201% compared to the B_4C-free FeNiCr coating, and up to 351% relative to the AISI 1040 steel substrate, respectively. This was promoted by the synergistic strengthening effect between the in situ formed Fe_2B and the retained B_4C phases.

(5) The comprehensive scratch test analysis demonstrated the enhanced wear resistance and robust mechanical properties of the FeNiCr-B_4C coatings. These coatings exhibit excellent adhesion, a beneficial hardness gradient, high cohesive strength, a degree of plasticity, and homogenous B_4C dispersion, all contributing to their overall durability.

Thus, optimized short-pulsed laser cladding, coupled with moderate B_4C (5 and 7 wt.%) reinforcement, presents a viable and promising approach to fabricate high-strength FeNiCr-B_4C MMC coatings for challenging engineering applications. Future studies should focus on analyzing the high-temperature behavior and application-specific performance (cavitation, abrasion, and corrosion resistance) of the FeNiCr-B_4C coatings. This comprehensive investigation represents a critical avenue for advancing our understanding of these coatings' potential in demanding environments and guiding future materials development efforts.

Author Contributions: Conceptualization, A.O. and O.I.; formal analysis, A.O., O.I., A.S., V.Z., E.M., K.L., J.L., T.S., A.M., Y.K. (Yury Korobov), E.K., I.Z., Y.K. (Yulia Korkh), T.K., P.W., and Y.J.; investigation, A.O., O.I., A.S., V.Z., E.M., K.L., J.L., T.S., A.M., Y.K. (Yury Korobov), E.K., I.Z., Y.K. (Yulia Korkh), T.K., P.W., and Y.J.; supervision, A.O. and O.I.; writing—original draft, A.O., O.I., A.S., V.Z., E.M., K.L., J.L., T.S., A.M., Y.K. (Yury Korobov), E.K., I.Z., Y.K. (Yulia Korkh), T.K., P.W., and Y.J.;

writing—review and editing, A.O., O.I., A.S., V.Z., E.M., K.L., J.L., T.S., A.M., Y.K. (Yury Korobov), E.K., I.Z., Y.K. (Yulia Korkh), T.K., P.W., and Y.J. All authors have read and agreed to the published version of the manuscript.

Funding: This research received no external funding.

Institutional Review Board Statement: Not applicable.

Informed Consent Statement: Not applicable.

Data Availability Statement: Data will be made available upon request.

Acknowledgments: This research was carried out within the state assignment of the Ministry of Science and Higher Education of the Russian Federation (themes "Structure" No. 122021000033-2; and "Spin" No. 122021000036-3) using the equipment of the Collaborative Access Center "Testing Center of Nanotechnology and Advanced Materials" of the IMP UB RAS and supported by the National Natural Science Foundation of China (Grant No. 52105351).

Conflicts of Interest: The authors declare no conflicts of interest.

References

1. Karmakar, R.; Maji, P.; Ghosh, S.K. A Review on the Nickel Based Metal Matrix Composite Coating. *Met. Mater. Int.* **2021**, *27*, 2134–2145. [CrossRef]
2. Sarmah, P.; Gupta, K. Recent Advancements in Fabrication of Metal Matrix Composites: A Systematic Review. *Materials* **2024**, *17*, 4635. [CrossRef] [PubMed]
3. Tiwari, V.; Mandal, V.; Sarkar, M.; Kumar, A.; Bhagyaraj, J.; Singh, M.K.; Mukherjee, S.; Mondal, K.; Ramkumar, J.; Jain, J.; et al. Enhanced mechanical properties and microstructure of TiC reinforced Stellite 6 metal matrix composites (MMCs) via laser cladding additive manufacturing. *J. Alloys Compd.* **2025**, *1010*, 178001. [CrossRef]
4. Marshall, P. *Austenitic Stainless Steels: Microstructure and Mechanical Properties*; Elsevier Applied Science: London, UK, 1984; Available online: https://link.springer.com/book/9780853342779 (accessed on 15 April 2025).
5. Brassart, L.H.; Besson, J.; Delloro, F.; Haboussa, D.; Delabrouille, F.; Rolland, G.; Shen, Y.; Gourgues-Lorenzon, A.-F. Effect of Various Heat Treatments on the Microstructure of 316L Austenitic Stainless Steel Coatings Obtained by Cold Spray. *J. Therm. Spray Technol.* **2022**, *31*, 1725–1746. [CrossRef]
6. Kaladhar, M.; Venkata Subbaiah, K.; Srinivasa Rao, C.H. Machining of austenitic stainless steels—A review. *Int. J. Mach. Mach. Mater.* **2012**, *12*, 178–192. [CrossRef]
7. Adrian Roberts, J.T. *Structural Materials in Nuclear Power Systems*; Plenum Press: New York, NY, USA, 1981.
8. Ehrlich, K.; Konys, J.; Heikinheimo, L. Materials for high performance light water reactors. *J. Nucl. Mater.* **2004**, *327*, 140–147. [CrossRef]
9. Takakuwa, O.; Ogawa, Y.; Yamabe, J.; Matsunaga, H. Hydrogen-induced ductility loss of precipitation-strengthened Fe-Ni-Cr-based superalloy. *Mater. Sci. Eng. A* **2019**, *739*, 335–342. [CrossRef]
10. Ehrnstén, U.; Andresen, P.L.; Que, Z. A review of stress corrosion cracking of austenitic stainless steels in PWR primary water. *J. Nucl. Mater.* **2024**, *588*, 154815. [CrossRef]
11. Hasanzadeh, A.; Hamedani, A.; Alahyarizadeh, G.; Minuchehr, A.; Aghaei, M. The Role of Chromium and Nickel on the Thermal and Mechanical Properties of FeNiCr Austenitic Stainless Steels under High Pressure and Temperature: A Molecular Dynamics Study. *Mol. Simul.* **2019**, *45*, 672–684. [CrossRef]
12. Washko, S.D.; Aggen, G. *Asm Handbook: Properties and Selection: Irons, Steels, and High-Performance Alloys*, 10th ed.; ASM International: Materials Park, OH, USA, 1990; Volume 1.
13. Balaji, S.; Upadhyaya, A. Mechanical, corrosion, and sliding wear behavior of intermetallics reinforced austenitic stainless steel composites. *J. Mater. Sci.* **2009**, *44*, 2310–2319. [CrossRef]
14. AlMangour, B.; Baek, M.-S.; Grzesiak, D.; Lee, K.-A. Strengthening of stainless steel by titanium carbide addition and grain refinement during selective laser melting. *Mater. Sci. Eng. A* **2018**, *712*, 812–818. [CrossRef]
15. Li, B.; Qian, B.; Xu, Y.; Liu, Z.; Zhang, J.; Xuan, F. Additive manufacturing of ultrafine-grained austenitic stainless steel matrix composite via vanadium carbide reinforcement addition and selective laser melting: Formation mechanism and strengthening effect. *Mater. Sci. Eng. A* **2019**, *745*, 495–508. [CrossRef]
16. Okulov, A.; Korobov, Y.; Stepchenkov, A.; Makarov, A.; Iusupova, O.; Korkh, Y.; Kuznetsova, T.; Kharanzhevskiy, E.; Liu, K. Mechanical and structural characterization of laser-cladded medium-entropy FeNiCr-B_4C coatings. *Materials* **2023**, *16*, 5479. [CrossRef] [PubMed]

17. Wang, H.; Li, J.; Liu, K.; Xu, G.; Zhu, H.; Wang, J.; Xu, C.; Wang, L.; Okulov, A. Microstructural evolution and corrosion resistance property of in-situ Zr–C(B, Si)/Ni–Zr reinforced composite coatings on zirconium alloy by laser cladding. *J. Mater. Res. Technol.* **2023**, *26*, 530–541. [CrossRef]
18. Okulov, A.; Iusupova, O.; Liu, K.; Li, J.; Stepchenkov, A.; Zavalishin, V.; Korkh, Y.; Kuznetsova, T.; Mugada, K.K.; Moganraj, A. Micromechanical and Tribological Performance of Laser-Cladded Equiatomic FeNiCr Coatings Reinforced with TiC and NbC Particles. *Materials* **2024**, *17*, 4686. [CrossRef]
19. Domnich, V.; Reynaud, S.; Haber, R.A.; Chhowalla, M. Boron Carbide: Structure, Properties, and Stability under Stress. *J. Am. Ceram. Soc.* **2011**, *94*, 3605–3628. [CrossRef]
20. Xie, K.Y.; Domnich, V.; Farbaniec, L.; Chen, B.; Kuwelkar, K.; Ma, L.; McCauley, J.W.; Haber, R.A.; Ramesh, K.T.; Chen, M.; et al. Microstructural characterization of boron-rich boron carbide. *Acta Mater.* **2017**, *136*, 202–214. [CrossRef]
21. Garcıa, J.; Collado Cipres, V.; Blomqvist, A.; Kaplan, B. Cemented carbide microstructures: A review. *Int. J. Refract. Met. Hard Mater.* **2019**, *80*, 40–68. [CrossRef]
22. Liang, D.; Zhao, C.; Zhu, W.; Wei, P.; Jiang, F.; Zhang, Y.; Sun, Q.; Ren, F. Overcoming the strength-ductility trade-off via the formation of nanoscale Cr-rich precipitates in an ultrafine-grained FCC CrFeNi medium entropy alloy matrix. *Mater. Sci. Eng. A* **2019**, *762*, 138107. [CrossRef]
23. Fu, A.; Liu, B.; Lu, W.; Liu, B.; Li, J.; Fang, Q.; Li, Z.; Liu, Y. A novel supersaturated medium entropy alloy with superior tensile properties and corrosion resistance. *Scr. Mater.* **2020**, *186*, 381–386. [CrossRef]
24. Liang, D.; Zhao, C.; Zhu, W.; Wei, P.; Jiang, F.; Ren, F. Significantly Enhanced Wear Resistance of an Ultrafine-Grained CrFeNi Medium-Entropy Alloy at Elevated Temperatures. *Metall. Mater. Trans. A* **2020**, *51*, 2834–2850. [CrossRef]
25. Schneider, M.; Laplanche, G. Effects of temperature on mechanical properties and deformation mechanisms of the equiatomic CrFeNi medium-entropy alloy. *Acta Mater.* **2021**, *204*, 116470. [CrossRef]
26. Zhou, Z.; Liu, B.; Guo, W.; Fu, A.; Duan, H.; Li, W. Corrosion behavior and mechanism of FeCrNi medium entropy alloy prepared by powder metallurgy. *J. Alloys Compd.* **2021**, *867*, 159094. [CrossRef]
27. Miranda, R.M.; Gandra, J.P.; Vilaca, P.; Quintino, L.; Santos, T.G. *Surface Modification by Solid State Processing*; Elsevier: Amsterdam, The Netherlands; Woodhead Publishing Limited: Sawston, UK, 2014. Available online: http://www.sciencedirect.com/science/book/9780857094681 (accessed on 10 April 2025).
28. Dezfuli, S.M.; Sabzi, M. Deposition of ceramic nanocomposite coatings by electroplating process: A review of layer-deposition mechanisms and effective parameters on the formation of the coating. *Ceram. Int.* **2019**, *45*, 21835–21842. [CrossRef]
29. Korobov, Y.; Antonov, M.; Astafiev, V.; Brodova, I.; Kutaev, V.; Estemirova, S.; Devyatyarov, M.; Okulov, A. Erosion Wear Behavior of HVAF-Sprayed WC/Cr_3C_2-Based Cermet and Martensitic Stainless Steel Coatings on AlSi7Mg0.3 Alloy: A Comparative Study. *J. Manuf. Mater. Process.* **2024**, *8*, 231. [CrossRef]
30. Yang, J.; Liu, F.; Miao, X.; Yang, F. Influence of laser cladding process on the magnetic properties of WC–FeNiCr metal–matrix composite coatings. *J. Mater. Process. Technol.* **2012**, *212*, 1862–1868. [CrossRef]
31. Yang, J.; Miao, X.; Wang, X.; Chen, H.; Yang, F. Microstructure, magnetic properties and empirical electron theory calculations of laser cladding FeNiCr/60%WC composite coatings with Mo additions. *Int. J. Refract. Met. Hard Mater.* **2016**, *54*, 216–222. [CrossRef]
32. Li, Y.; Dong, S.; He, P.; Yan, S.; Li, E.; Liu, X.; Xu, B. Microstructure characteristics and mechanical properties of new-type FeNiCr laser cladding alloy coating on nodular cast iron. *J. Mater. Process. Technol.* **2019**, *269*, 163–171. [CrossRef]
33. Zhu, L.; Xue, P.; Lan, Q.; Meng, G.; Ren, Y.; Yang, Z.; Xu, P.; Liu, Z. Recent research and development status of laser cladding: A review. *Opt. Laser Technol.* **2021**, *138*, 106915. [CrossRef]
34. Gokhfeld, N.V.; Okulov, A.V.; Filippov, M.A.; Estemirova, S.K.; Korobov, Y.S.; Morozov, S.O. The Comparative Analysis of the Fe–Cr–C–Ti–Al Coatings Synthesized by Laser, Arc and Hybrid Cladding Methods. *Phys. Solid State* **2022**, *64*, 356–361. [CrossRef]
35. Okulov, A.V.; Iusupova, O.S.; Liu, K. Development of multicomponent hybrid powders based on titanium and niobium carbides as a promising material for laser cladding. *E3S Web Conf.* **2023**, *413*, 4012. [CrossRef]
36. Wang, L.; Liu, K.; Li, J.; Chen, Z.; Wang, J.; Okulov, A. Interfacial microstructure and mechanical properties of diffusion bonded joints of additive manufactured 17-4 PH stainless steel and TC4 titanium alloy. *Vacuum* **2024**, *219*, 112709–112716. [CrossRef]
37. Kishor, G.; Mugada, K.K.; Mahto, R.P.; Okulov, A. Assessment of microstructure development, defect formation, innovations, and challenges in wire arc based metal additive manufacturing. *Proc. Inst. Mech. Eng. Part L* **2024**. [CrossRef]
38. Giurlani, W.; Zangari, G.; Gambinossi, F.; Passaponti, M.; Salvietti, E.; Benedetto, F.D.; Caporali, S.; Innocenti, M. Electroplating for Decorative Applications: Recent Trends in Research and Development. *Coatings* **2018**, *8*, 260. [CrossRef]
39. Sathish, M.; Radhika, N.; Saleh, B. Duplex and Composite Coatings: A Thematic Review on Thermal Spray Techniques and Applications. *Met. Mater. Int.* **2023**, *29*, 1229–1297. [CrossRef]
40. Alizadeh-Sh, M.; Marashi, S.P.H.; Ranjbarnodeh, E.; Shoja-Razavi, R.; Oliveira, J.P. Prediction of solidification cracking by an empirical-statistical analysis for laser cladding of Inconel 718 powder on a non-weldable substrate. *Opt. Laser Technol.* **2020**, *128*, 106244. [CrossRef]

41. Liu, K.; Wang, H.; Li, J.; Geng, S.; Chen, Z.; Okulov, A. A Review on Factors Infuencing Solidifcation Cracking of Magnesium Alloys During Welding. *Met. Mater. Int.* **2024**, *30*, 1723–1742. [CrossRef]
42. *ISO 14577-1:2015*; Metallic Materials—Instrumented Indentation Test for Hardness and Materials Parameters—Part 1: Test Method. International Organization for Standardization (ISO): Geneva, Switzerland, 2015. Available online: https://www.iso.org/standard/56626.html (accessed on 12 April 2025).
43. Dong, X.L.; Zhang, Z.D.; Xiao, Q.F.; Zhao, X.G.; Chuang, Y.C.; Jin, S.R.; Sun, W.M.; Li, Z.J.; Zheng, Z.X.; Yang, H. Characterization of ultrafine γ-Fe(C), α-Fe(C) and Fe_3C particles synthesized by arc-discharge in methane. *J. Mater. Sci.* **1998**, *33*, 1915–1919. [CrossRef]
44. Campos, I.; Ramírez, G.; Figueroa, U.; Martínez, J.; Morales, O. Evaluation of boron mobility on the phases FeB, Fe_2B and diffusion zone in AISI 1045 and M2 steels. *Appl. Surf. Sci.* **2007**, *253*, 3469–3475. [CrossRef]
45. Kartal, G.; Timur, S.; Sista, V.; Eryilmaz, O.L.; Erdemir, A. The growth of single Fe_2B phase on low carbon steel via phase homogenization in electrochemical boriding (PHEB). *Surf. Coat. Technol.* **2011**, *206*, 2005–2011. [CrossRef]
46. Guo, H.; Zhao, Y.; Xu, S.; Li, J.; Liu, N.; Zhang, Y.; Zhang, Z. Influence of high B_4C contents on structural evolution of Al-B_4C nanocomposite powders produced by high energy ball milling. *Ceram. Int.* **2019**, *45*, 5436–5447. [CrossRef]
47. Faria, D.L.A.; Silva, S.V.; Oliveir, M.T. Raman microspectroscopy of some iron oxides and oxyhydroxides. *J. Raman Spectrosc.* **1997**, *28*, 873–878. [CrossRef]
48. Kim, J.; Choi, K.J.; Bahn, C.B.; Kim, J.H. In situ Raman spectroscopic analysis of surface oxide films on Ni-base alloy/low alloy steel dissimilar metal weld interfaces in high-temperature water. *J. Nucl. Mater.* **2014**, *449*, 181–187. [CrossRef]
49. Yan, X.Q.; Li, W.J.; Goto, T.; Chen, M.W. Raman spectroscopy of pressure-induced amorphous boron carbide. *Appl. Phys. Lett.* **2006**, *88*, 131905. [CrossRef]
50. Kunka, C.; Awasthi, A.; Subhash, G. Evaluating boron-carbide constituents with simulated Raman spectra. *Scr. Mater.* **2017**, *138*, 32–34. [CrossRef]
51. Brown-Shaklee, H.J.; Neuman, E.W.; Fahrenholtz, W.G.; Hilmas, G.E. Optical characterization of boron carbide powders synthesized with varying B-to-C ratios. *J. Am. Ceram. Soc.* **2023**, *106*, 1932–1944. [CrossRef]
52. Cheng, Y.T.; Cheng, C.M. Relationships between hardness, elastic modulus and the work of indentation. *Appl. Phys. Lett.* **1998**, *73*, 614. [CrossRef]
53. Mayrhofer, P.H.; Mitterer, C.; Musil, J. Structure-property relationships in single- and dual-phase nanocrystalline hard coatings. *Surf. Coat. Technol.* **2003**, *174–175*, 725–731. [CrossRef]
54. Freitas Rodrigues, P.; Teixeira, R.S.; Le Sénéchal, N.V.; Braz Fernandes, F.M.; Paula, A.S. The Influence of the Soaking Temperature Rotary Forging and Solution Heat Treatment on the Structural and Mechanical Behavior in Ni-Rich NiTi Alloy. *Materials* **2022**, *15*, 63. [CrossRef]
55. Page, T.F.; Hainsworth, S.V. Using nanoindentation techniques for the characterization of coated systems: A critique. *Surf. Coat. Technol.* **1993**, *62*, 201–208. [CrossRef]
56. Petrzhik, M.I.; Levashov, E.A. Modern methods for investigating functional surfaces of advanced materials by mechanical contact testing. *Crystallogr. Rep.* **2007**, *52*, 966–974. [CrossRef]
57. Milman, Y.V.; Chugunova, S.I.; Goncharova, I.V.; Golubenko, A.A. Plasticity of Materials Determined by the Indentation Method. *Usp. Fiz. Met.* **2018**, *19*, 271–307. [CrossRef]

Disclaimer/Publisher's Note: The statements, opinions and data contained in all publications are solely those of the individual author(s) and contributor(s) and not of MDPI and/or the editor(s). MDPI and/or the editor(s) disclaim responsibility for any injury to people or property resulting from any ideas, methods, instructions or products referred to in the content.